Sustainable Energy & Fuels

Effect of ZnO and PEDOT:PSS Charge Selective Layers on Photovoltage of Cuprous Oxide (Cu_2O) Heterojunction Solar Cells

Journal:	*Sustainable Energy & Fuels*
Manuscript ID	SE-ART-03-2024-000416.R1
Article Type:	Paper
Date Submitted by the Author:	16-Apr-2024
Complete List of Authors:	Li, Jiajun; University of California, Department of Chemistry Mendoza, Hervin; University of California, Department of Chemistry Kundmann, Anna; University of California, Department of Chemistry Osterloh, Frank ; University of California, Department of Chemistry

Effect of ZnO and PEDOT:PSS Charge Selective Layers on Photovoltage of Cuprous Oxide (Cu_2O) Heterojunction Solar Cells

Jiajun Li, Hervin Errol T. Mendoza, Anna Kundmann, and Frank E. Osterloh*

Department of Chemistry, University of California, Davis. One Shields Avenue, Davis, CA, 95616, USA. Fax: (+1)530 752 8995; E-mail: fosterloh@ucdavis.edu.

Abstract

Electrochemical deposition (ECD) of Cu_2O provides a scalable and low temperature pathway to solar cells with a theoretical high energy conversion efficiency of 23%, based on the 2.0-2.2 eV band gap of Cu_2O. However, existing ECD-Cu_2O devices are plagued by poor crystallinity and low selectivity of the electron and hole transport layers. Here we use Vibrating Kelvin Probe Surface Photovoltage Spectroscopy (VKP-SPV) to probe the charge transfer selectivity in FTO/ZnO/Cu_2O/PEDOT:PSS/Ni heterojunction solar cells. Selective electron extraction is achieved at the ZnO back contact to Cu_2O, as confirmed by a negative surface photovoltage signal. While the uncoated Cu_2O surface is electron-selective due to the formation of a hole depletion layer, spin coating of a PEDOT:PSS film turns it into a hole-selective interface. After adding nickel metal ink top electrodes, functional 1.0 cm^2 solar cells with power conversion efficiency (PCE) of up to 0.07 %,195 mV open-circuit voltage, and 1.28 mA/cm^2 short-circuit photocurrent are achieved. The photovoltaic performance is higher for aluminum doped zinc oxide (AZO) substrates than for fluorine doped tin oxide (FTO) due to the presence of a n-/p-junction that further increases the electron selectivity of the AZO/ZnO/Cu_2O contacts. Overall, this work demonstrates the first application of PEDOT:PSS as a hole transport layer (HTL) for Cu_2O and the use of VKP-SPV to measure the photovoltage contributions of the Cu_2O interfaces. The ability to fabricate Cu_2O solar cells at near room temperature without the use of vacuum methods or rare elements is an important step towards a scalable Cu_2O PV technology.

Introduction

Avoiding the most detrimental effects of climate change demands a rapid increase in the deployment rate of solar energy conversion devices.[1] However, commercial photovoltaic cells utilize just a handful of semiconductors, incl. silicon, gallium arsenide, copper gallium indium sulfide, cadmium telluride, lead halide perovskite, and organic polymers, [2] which leaves considerable room for improvements. Emerging inorganic photovoltaic absorber materials such as binary and ternary chalcogenides [3, 4] offer comparable efficiencies and may be easier to produce on a large scale because no vacuum methods are required.[5, 6] The relatively high abundance of copper makes cuprous oxide (Cu_2O) another promising photovoltaic absorber. [7-9] Based on its 2.0 - 2.2 eV bandgap, Cu_2O cells can achieve up to 23% solar power conversion efficiency (PCE) [7, 9, 10] and photovoltaic quality Cu_2O films can be grown by electrochemical deposition (ECD) from aqueous solutions.[11-14] In ECD, semiconductor films are formed by electrochemical reduction or oxidation of soluble precursors.[8, 11, 13, 15-18] This allows control over the growth rate via the current and the applied potential, and over doping levels by adjusting the electrolyte pH and metal ion concentration.[14, 19-22] Because the reaction involves electron transfer from the conductive substrate, conformal films can be grown over large areas, often at near room temperature. For example, *British Petroleum* used ECD for the manufacture of CdTe solar cell modules 0.94 m^2 in size (*Apollo process*). [23] Several groups also have reported Cu_2O photovoltaics made by ECD. [11-14, 24] However, to date, the performance of ECD Cu_2O cells does not yet reach that of thermally grown Cu_2O (3.83-6%).[12, 25, 26] That is mainly due to the lower crystallinity and lower charge mobility (5 $cm^2 V^{-1} s^{-1}$) of ECD Cu_2O compared to thermally grown Cu_2O (100 $cm^2 V^{-1} s^{-1}$). [7] Also, the light penetration depth of Cu_2O is quite large (>

2 μm at 600 nm) which necessitates relatively thick and highly crystalline films for complete light absorption and charge carrier extraction.[7] Finally, electrical contacts to Cu_2O often generate Cu(0), which limits the efficiency of junctions and causes photovoltage loss. [27]

To obtain further insight into these limitations, we use Vibrating Kelvin Probe-Surface Photovoltage Spectroscopy (VKP-SPV) as a tool to probe photochemical charge separation at ECD-grown Cu_2O heterojunctions. This is done on Cu_2O heterojunction photovoltaic cells that employ the superstrate device architecture shown in **Figure 1.** [12, 13, 24] Here, ZnO serves as an electron transport layer (ETL) and Poly(3,4-ethylenedioxythiophene): poly(4-styrene sulfonate) (PEDOT:PSS) is used as a HTL. ZnO is well suited as ETL for Cu_2O because of its wide band gap of 3.37 eV and high electron mobility of ~120 $cm^2V^{-1}s^{-1}$.[13] PEDOT:PSS is widely applied as a HTL in organic photovoltaic devices [28, 29] and inorganic solar cells [30-32] because of its large work function (5.0 - 5.2 eV), p-type character, and high hole conductivity. [33, 34] However, this is the first example of using this HTL in combination with Cu_2O. Functioning 1.0 cm^2 Cu_2O solar cells are obtained after applying painted nickel ink as the top electrode. As we will show in the following, the performance of these devices is limited by pinholes in the Cu_2O layers, high series resistance of the ZnO/Cu_2O/PEDOT:PSS stack, and electron trapping at the Cu_2O/PEDOT:PSS interface. Importantly, the charge selectivity of the Cu_2O contacts can be observed with VKP-SPV, allowing a better understanding of the factors that control charge separation and energy conversion with Cu_2O solar cells.

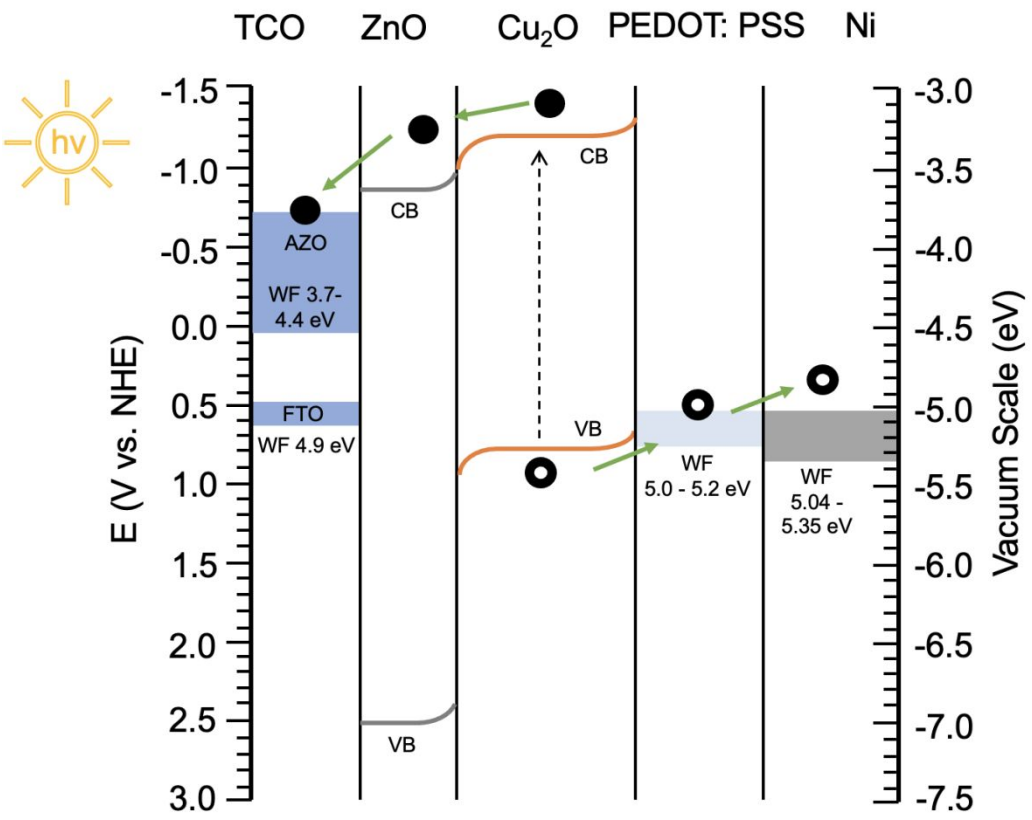

Figure 1. Energy diagram for FTO/ZnO/Cu_2O/PEDOT:PSS/Ni, showing values for work function (WF), band edges (CB and VB), and Fermi Levels (E_f).

Results and Discussion

Cu_2O photovoltaic devices were fabricated as shown in **Figure 2**. The first step consists of electrochemical deposition of the ZnO electron transport layer (ETL) onto a 1.00 cm^2 area of a commercial fluorine doped tin oxide (FTO) or aluminum doped zinc oxide (AZO) substrate, as previously described by Ghannam et al. [35] This is achieved by applying a cathodic bias of -0.90 V vs SCE to a $5.0x10^{-3}$ M $Zn(NO_3)_2$ electrolyte at 70 °C, resulting in reduction of nitrate to nitrite and the formation of hydroxide, as shown in **equation 1**.

The formed hydroxide then precipitates $Zn(OH)_2$ on the working electrode (**equation 2**), which dehydrates to form crystalline ZnO (**equation 3**).

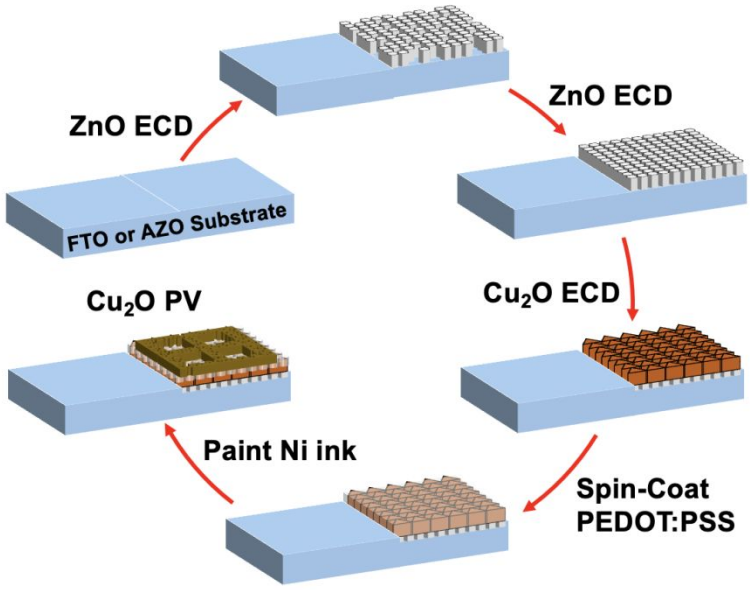

Figure 2. Device fabrication scheme.

$$NO_3^- + H_2O + 2e^- \rightarrow NO_2^- + 2\ OH^- \quad \text{(Eq.1)}$$

$$Zn^{2+} + 2\ OH^- \rightarrow Zn(OH)_2 \quad \text{(Eq.2)}$$

$$Zn(OH)_2 \rightarrow ZnO + H_2O \quad \text{(Eq.3)}$$

$$Cu^{2+} + e^- \rightarrow Cu^+ \quad \text{(Eq.4)}$$

$$2\ Cu^+ + 2\ OH^- \rightarrow Cu_2O + H_2O \quad \text{(Eq.5)}$$

To facilitate this dehydration reaction, the bath temperature was maintained at 70 °C. To reduce the concentration of residual pinholes, the electrodeposition process was repeated once more with the same pre-step voltage of -1.20 V and applied voltage of -0.90 V vs SCE. **Figure 3a** and **3d** show photos of the semi-transparent ZnO films on FTO

and AZO, respectively. ZnO films cover a 1x1 cm^2 area of the substrate and appear milky white due to light scattering.

As the next step, Cu_2O is electrochemically deposited at -0.25 V to -0.40 V vs SCE from 0.40 M copper sulfate solution at 60 °C. This potential was chosen to maintain a steady current of approximately -0.80 mA. In the electrochemical synthesis of Cu_2O, lactate (2-hydroxypropanoic acid anion) is used as a complexing agent for the Cu(2+) ions. This prevents the precipitation of copper hydroxide ($Cu(OH)_2$) under basic conditions of the experiment. Upon reaching the electrode surface, Cu^{2+} ions undergo reduction to Cu^{+} followed by deposition of Cu_2O. The specific temperature of 60 °C was selected to promote the formation of Cu_2O with larger grain sizes and to reduce electrical resistivity, as indicated in previous studies. [36] The pH of the solution was maintained at pH = 12 to ensure the p-type conductivity of the deposited Cu_2O. It is well-documented that Cu_2O synthesized under acidic conditions tends to exhibit n-type behavior. [36] **Figures 3b** and **3c** show the characteristic purple-red color of Cu_2O on ZnO on both FTO and AZO substrates, respectively. In the next fabrication step, a PEDOT:PSS layer was deposited by spin coating in air, followed by air-drying. **Figure 3c** shows the non-uniformity of the PEDOT:PSS film, seen as a dark region on the bottom of the photo. Due to its low contrast, PEDOT:PSS was not observable by scanning electron microscopy (SEM), but could be confirmed by energy dispersive X-ray spectroscopy (EDX). As seen in **Figure S1**, all elements (carbon, oxygen, and sulfur) could be detected. To finalize the device, a network of nickel (Ni) contacts was painted on the film using a fine brush. As illustrated in **Figure 3f**, these metal contacts exhibit a rough surface texture. The non-uniformity of these metal contacts presents potential sources of defects, while their increased thickness prevents

light from reaching the Cu_2O absorber. Therefore, these devices rely on illumination through the transparent FTO/AZO substrate. To observe the morphology and structure of the films, SEM images and X-ray diffraction (XRD) patterns were recorded. The ZnO nanorods are approximately 200 nm in diameter and 1 micrometer long, as shown in **Figures 4b and 4c**.

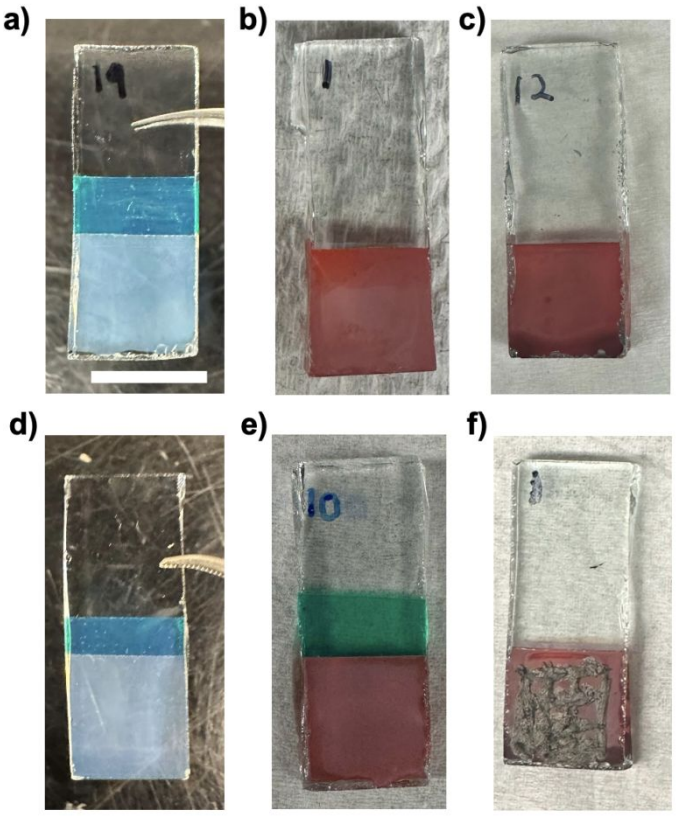

Figure 3. Photos of a) FTO/ZnO, b) FTO/ZnO/Cu_2O, c) FTO/ZnO/Cu_2O/PEDOT:PSS and d) AZO/ZnO, e) AZO/ZnO/Cu_2O, f) AZO/ZnO/Cu_2O/PEDOT:PSS/Ni. The blue and green regions are masking tape and the scale bar is 1.0 cm.

XRD patterns of the films (**Figure 5**) confirm the wurtzite structure of ZnO. Based on the enhanced (002) peak, the ZnO film in Figure **5b** has a preferential orientation of the c axis

perpendicular to the FTO substrate. This agrees with the observed vertical orientation of the hexagonal nanorods in **Figure 4b**. Interestingly, ZnO nanoplates with a preferred (100) growth direction become accessible by increasing the $Zn(NO_3)_2$ concentration in the electrolyte tenfold to 0.05 M $Zn(NO_3)_2$. These plates can be identified in the SEM in **Figure 4a** and in the XRD in **Figure 5a.** According to Pradhan et al. [37] the (100) directional growth at high zinc nitrate concentrations is a result of the fast formation of $Zn(OH)_2$ as an intermediate to ZnO.

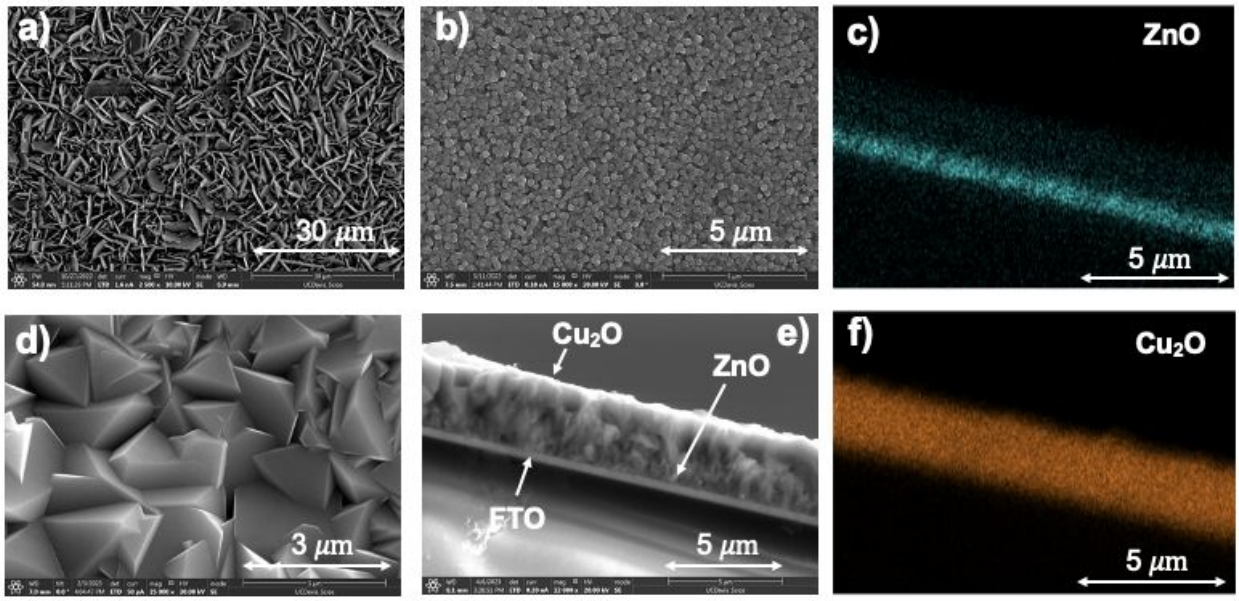

Figure 4. SEM images for a) ZnO nanoplates deposited on FTO from 0.05 M $Zn(NO_3)_2$ at -0.90 V vs SCE, b) ZnO nanorod array on FTO from $5.0x10^{-3}$ M $Zn(NO_3)_2$ at -0.90 V vs SCE, and d) Cu_2O film on FTO/ZnO from 0.4 M $CuSO_4$ at -0.3 V vs SCE. Cross section SEM image of e) FTO/Cu_2O/ZnO heterostructure, and EDX images for c) and f) ZnO and Cu_2O, respectively.

SEM images of the FTO/ZnO/Cu_2O stacks are shown in **Figures 4d** and **e**. They confirm the presence of a uniform Cu_2O film composed of truncated octahedral structures with an

average crystal size of about 5 μm. This morphology is similar to that reported by Paracchino et al. [36] Powder XRD patterns in **Figure 5c** and **d** confirm the cuprite structure type, and reveal that on AZO/FTO, the Cu_2O grains grow preferentially in the [111] direction, whereas no preferential orientation is seen on FTO/ZnO, based on the relative intensities of the (110), (111), and (200) peaks. [38] Based on cross section SEM images and elemental maps in **Figure 4c, 4e,** and **4f**, the Cu_2O layer is ~ 3 μm thick and forms a well-defined phase boundary with ZnO.

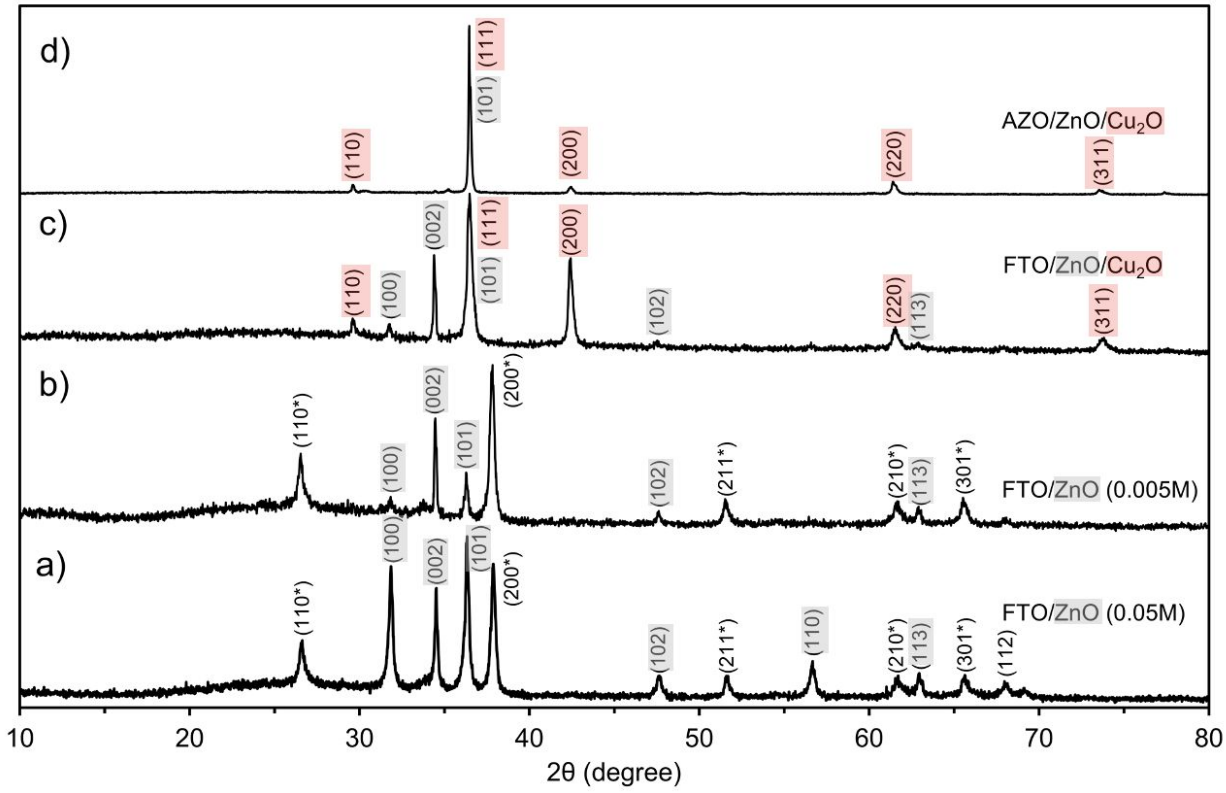

Figure 5. X-ray diffraction patterns of ZnO grown on FTO from a) 0.05 M $Zn(NO_3)_2$ or b) $5.0x10^{-3}$ M $Zn(NO_3)_2$ electrolyte. c) XRD patterns of FTO/ZnO/Cu_2O, and d) of AZO/ZnO/Cu_2O films. Miller indices marked * are from FTO. Peak assignments for Cu_2O and ZnO are from Ho et al. [38] and Pradhan et al, [37] respectively. The disappearance of the ZnO diffraction peaks in d) is due to shading of the X-rays by the thick Cu_2O overlayer.

Diffuse reflectance spectra for the stacks are summarized in **Figure 6**. The ZnO films on AZO and FTO have absorption onsets at 380 nm (3.26 eV) or 390 nm (3.18 eV), characteristic of the known band gap of ZnO (3.37 eV). [13] The ZnO/Cu_2O bilayers for both AZO and FTO substrates show the absorption edge at 625-640 nm (1.98 - 1.94 eV), slightly below the known band gap of Cu_2O (2.0 - 2.2 eV). [7] The absorption of ZnO is no longer observed because of shading from the Cu_2O layer. Spectra for the PEDOT:PSS coated stacks (**Figure S2**) are similar to the FTO/ZnO/Cu_2O and AZO/ZnO/Cu_2O samples, except for a small shift of the absorption onset to 640-655 nm (1.94 -1.89 eV). This is a result of the smaller bandgap of PEDOT:PSS (1.76 eV). [39]

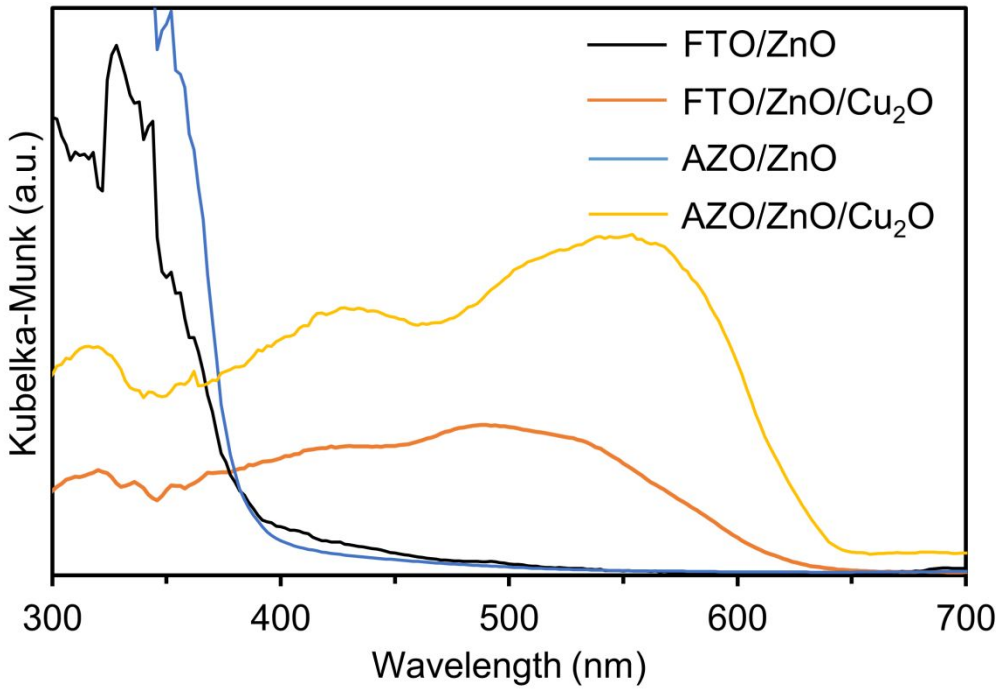

Figure 6. Diffuse reflectance optical spectra for FTO/ZnO, FTO/ZnO/Cu_2O, AZO/ZnO, and AZO/ZnO/Cu_2O. The weak visible absorption of the AZO/ZnO and FTO/ZnO samples is an artefact of

the diffuse reflectance measurement. It is attributed to transmission losses resulting from the thin ZnO film.

To probe the ability of the films to generate a photovoltage, Vibrating Kelvin Probe Surface Photovoltage spectroscopy (VKP-SPS) was applied. In VKP-SPV, the surface photovoltage signal–the change in the contact potential difference (CPD)–under illumination (SPV = CPD(light) - CPD(dark)) is measured with a vibrating Kelvin probe, as shown in **Figure 7a**. The SPV signal provides the direction of carrier separation and the effective bandgap of semiconductors. [40-42] For sufficiently conductive samples that are in electrochemical equilibrium in the dark (constant E_F), the SPV signal equals the photovoltage, i.e. the open circuit potential of the corresponding solar cell. [43-46] SPV spectra for ZnO/CuO_2 films on FTO and AZO are shown in **Figure 8a and 8b**.

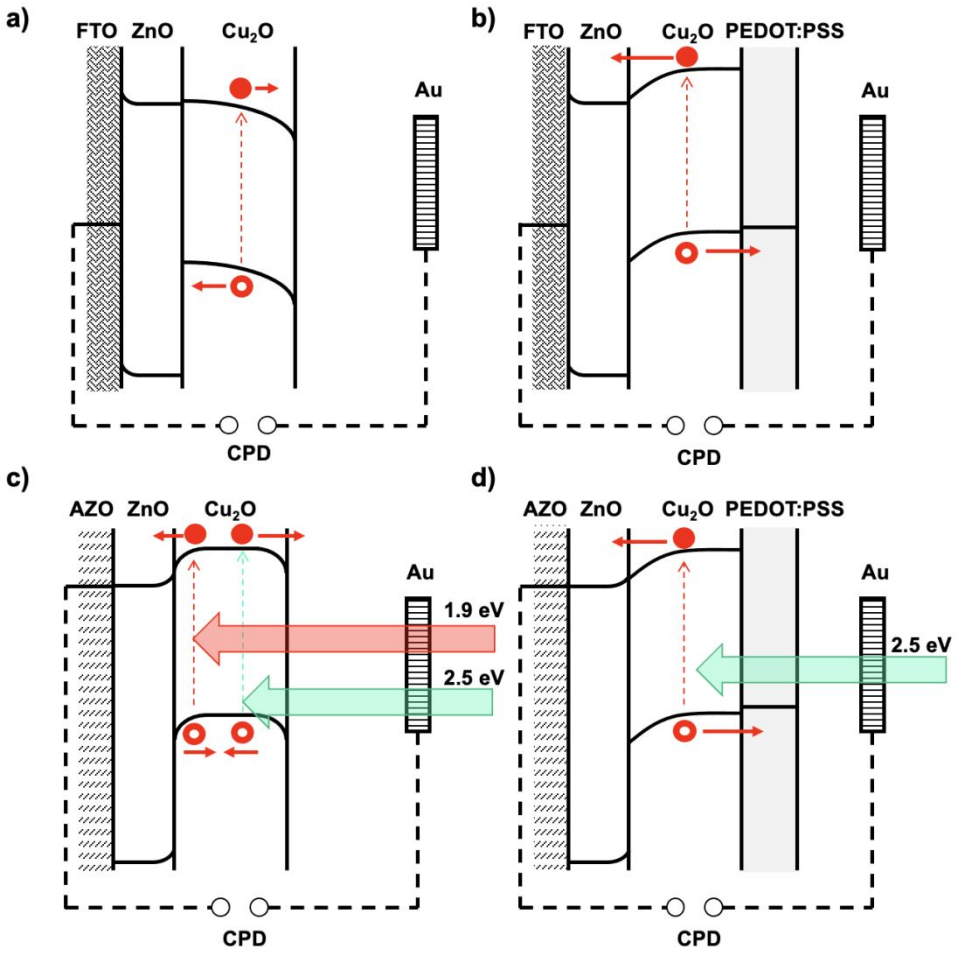

Figure 7. Charge separation scheme for a) FTO/ZnO/Cu_2O, b) FTO/ZnO/Cu_2O/ PEDOT:PSS, c) AZO/ZnO/Cu_2O, and d) AZO/ZnO/Cu_2O/PEDOT:PSS.

The major photovoltage onset occurs near 2.2 eV, slightly above the optical band gap value of Cu_2O (2.0 eV). This confirms that the SPV signal is due to excitation of Cu_2O, but also shows that photochemical charge separation in Cu_2O is not efficient in the 2.0-2.2 eV photon energy range. Both FTO and AZO substrates yield positive photovoltage, indicating that electrons (minority carriers) are moving towards the Kelvin probe, as shown in **Figure 7a**. This indicates that charge carrier separation is controlled by the hole depletion layer at the Cu_2O surface. However, the positive signal decreases significantly after adding the hole transfer layer PEDOT:PSS to the Cu_2O surface. This suggests a

reduction in band bending at the Cu_2O/PEDOT:PSS interface. Indeed, because of its high work function (5.0 - 5.2 eV) [33, 34] PEDOT:PSS is expected to form an ohmic contact with Cu_2O (**Figure 7b**). SPV spectra for Cu_2O films deposited on AZO substrates are similar (**Figure 8b**), except that the main positive SPV signal is preceded by *negative* SPV signals at 1.2-2.2 eV. A similar SPV inversion has been previously observed for junctions formed at n-Si/p-GaN and Au/n-$SrTiO_3$ interfaces. [47, 48] The signal is due to charge carriers moving in the Cu_2O depletion region at the n-ZnO/p-Cu_2O contact, as shown in the energy diagram in **Figure 7c**. Because light with energy below 2.0 eV can penetrate the Cu_2O layer, it can excite interfacial states near the Cu_2O back contact and probe the band bending there. The n-ZnO/p-Cu_2O junction is a result of the reducing workfunction of AZO (~ 3.7 – 4.4 eV), [49] which moves the ZnO Fermi level to more reducing potentials. This is not seen for the FTO/ZnO/Cu_2O contact because the FTO workfunction (4.9 eV) is more oxidizing than AZO. [50] The spectra in **Figure 8b** also reveal that the negative photovoltage (and the band bending at the n-ZnO/p-Cu_2O contact) increases in order AZO/Cu_2O < AZO/ZnO/Cu_2O < AZO/ZnO/Cu_2O/PEDOT:PSS. This reflects the increasing workfunction difference between the back and front of these multilayer configurations. The electron selectivity of the ZnO/Cu_2O contact is key to the operation of the solar cell in **Figure 1**. The SPV results show that this electron selectivity it is not only enabled by the deep valence band of the ZnO layer, which rejects photoholes (**Figure 1**), but also by the n-/p-junction at the ZnO/Cu_2O interface, which creates an electrostatic barrier for hole transfer.

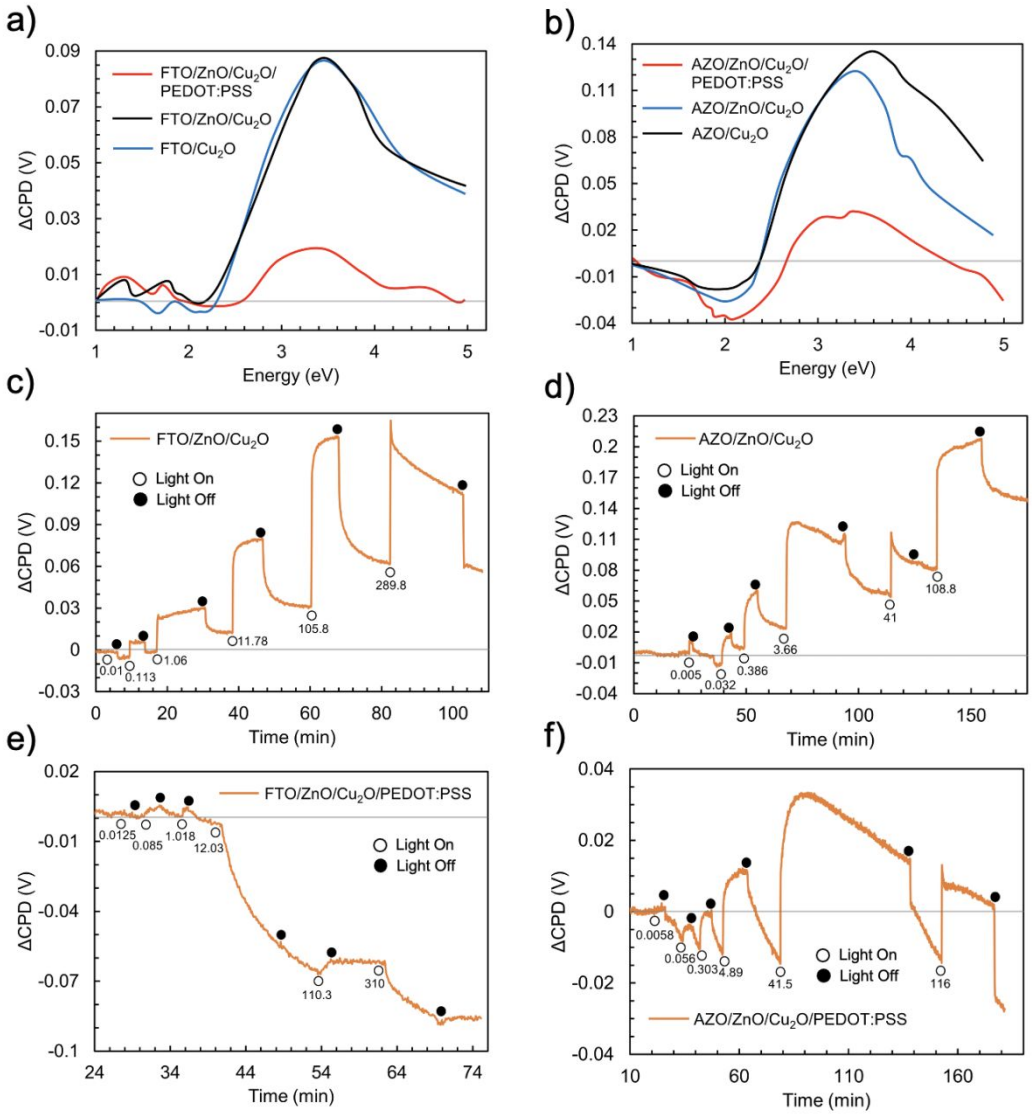

Figure 8. a) SPV spectra for FTO/Cu_2O, $FTO/ZnO/Cu_2O$, $FTO/ZnO/Cu_2O$/PEDOT:PSS and for b) AZO/Cu_2O, $AZO/ZnO/Cu_2O$, $AZO/ZnO/Cu_2O$/PEDOT:PSS. SPV under intermittent illumination for c) $FTO/ZnO/Cu_2O$, d) $AZO/ZnO/Cu_2O$, e) $FTO/ZnO/Cu_2O$/PEDOT:PSS, f) $AZO/ZnO/Cu_2O$/PEDOT:PSS. Numerical values indicate the irradiance (mW/cm^2) of the LED light (400 nm) at the sample.

Lastly, the rough (large) interface between the ZnO and Cu_2O layers (**Figure 4b**) favors the transfer of minority carriers, whose shorter lifetime reduces their diffusion length, compared to the longer-lived majority carriers (holes). [51, 52] Conversely, the positive SPV signal at > 2.4 eV is mainly due to excitation of the Cu_2O front contact, as shown in **Figure**

7c. This signal decreases considerably with the addition of PEDOT:PSS, as seen before for the FTO deposited films. This confirms that PEDOT:PSS promotes hole collection from Cu_2O. Without PEDOT:PSS, charge separation at the Cu_2O front would be controlled by a p-type depletion layer, as shown in **Figure 7a and 7c**, resulting in a dysfunctional device.

To better observe charge separation near the Cu_2O/PEDOT:PSS contact, SPV experiments were repeated with higher light intensities at a fixed wavelength of 400 nm (3.1 eV). This light predominantly probes the top Cu_2O contact, due to the short optical penetration depth ($1/\alpha$ = 40 nm) of Cu_2O at this wavelength (α = 2.5 x 10^5 cm^{-1} at 400 nm). [53] SPV signals in **Figures 8c - f** increase with light intensity, but show low reversibility, based on the residual SPV signal after turning off the light. For example, 90% of the SPV signal in **Figure 8e** remains after illuminating the FTO/ZnO/Cu_2O/PEDOT:PSS stack with 12.03 mW cm^{-2} light. That shows that charge carriers get trapped at the Cu_2O interfaces, likely in defects arising from dangling bonds and surface states.[54, 55] Again, both FTO/ZnO/Cu_2O and AZO/ZnO/Cu_2O structures show positive photovoltage that agrees with the charge separation schemes in **Figure 7a and 7c**. The native Cu_2O surface is electron selective, due to the formation of a p-type depletion layer. However, after addition of the PEDOT:PSS films (**Figure 8ef**), positive photovoltage values are diminished in size or even inverted. For example, the AZO/ZnO/Cu_2O/PEDOT:PSS stack in **Figure 8f** gives a diminished positive photovoltage of only 0.05 mV at 116 mW cm^{-2}, compared to 220 mV at 108.8 mW cm^{-2} for the AZO/ZnO/Cu_2O stack. And for FTO/ZnO/Cu_2O/PEDOT:PSS, the SPV under 12.03 mW cm^{-2} in **Figure 8e** is now negative (- 70 mV). While the differences between the data in **Figures 8e** and **f** are

attributed to variations in PEDOT:PSS coverage, and are not diagnostic, the comparison with **Figures 8cd** prove that the polymer removes the Cu_2O band bending at the surface and turns it into a flat band. This is shown in the energy diagrams in **Figure 7b and 7d.** Accordingly, electron-hole separation in Cu_2O does not take place at the Cu_2O interface with PEDOT:PSS, as demonstrated by the absence of a strong negative SPV signal, but at the interface to the ZnO ETL.

Finally, **Figure 9** shows representative current-voltage (I-V) curves for the completed FTO- and AZO-grown devices. In the dark, devices exhibit rectifying behavior based on the shape of the I-V plot. In both cases, the rectification stems from the ZnO/Cu_2O heterojunction (**Figure 1**). To assess the photovoltaic effect, devices were illuminated with simulated sunlight from a Xe arc lamp (100 mW cm^{-2}) through the transparent FTO or AZO substrate (Data in **Tables 1** and **S3-4**).

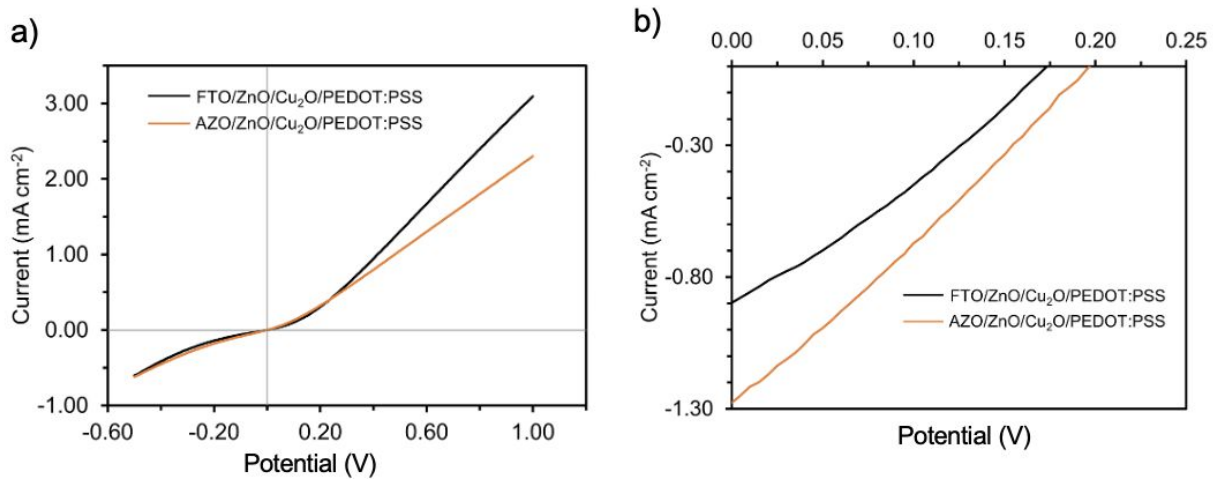

Figure 9. Current density versus applied potential (versus FTO/AZO counter electrode) in the dark (a) and (b) under simulated AM 1.5 illumination.

I-V curves in **Figure 9b** exhibit the expected shift to negative current. The FTO device reveals a short circuit current density (J_{SC}) of 0.90 mA/cm^2, an open circuit voltage (V_{OC})

of 160 mV, and a fill factor of 27.1%. Cells on the AZO substrate yield almost 1.5 times the J_{SC} (1.28 mA/cm^2), a higher V_{OC} (195 mV), and a higher power conversion efficiency (PCE; 0.07%). The improved performance can be attributed to the n-ZnO/p-Cu_2O junction as mentioned in the discussion of the SPV data. This junction exists only in the AZO based devices and aids the electron selectivity of the ZnO/Cu_2O contact. However, the hole selective PEDOT:PSS contact is also required. Without it, the FTO/ZnO/Cu_2O/Ni device only gives a very small photocurrent of 1 μA (**Table 1**). No net charge separation is achieved because of the opposing polarity of the junctions at the two Cu_2O interfaces (energy diagram in **Figure 7c**).

Table 1. Photovoltaic properties of Cu_2O solar cells under AM 1.5 illumination.

Sample	Jsc (mA/cm^2)	Voc (V)	FF (%)	PCE
FTO/ZnO/Cu_2O/Ni	0.001 ± 0.001	0.20 ± 5.68	-	-
FTO/ZnO/Cu_2O/PEDOT:PSS/Ni	0.90 ± 0.09	0.16 ± 3.19	27.06 ± 2.56	0.039 ± 0.004%
AZO/ZnO/Cu_2O/PEDOT:PSS/Ni	1.28 ± 0.14	0.20 ± 7.40	27.24 ± 0.90	0.068 ± 0.01%

The I-V data also reveals low fill factors and PCE for all devices. This is attributed to the presence of pinholes in the 1.00 cm^2 devices, as evidenced by the positive slope in the reverse bias direction. The inverse relationship between solar energy conversion performance and area size is well established in the field.[3, 56] The low photocurrent of the devices can be attributed to a high series resistance, which follows from the low slope of the I-V curve under forward bias. Lastly, electron trapping at the Cu_2O/PEDOT:PSS interface is an issue, as seen in the SPV data in **Figure 8f**. The problem may be overcome

with other HTLs. Lastly, the data in **Figure S5** shows that photocurrents and open circuit voltages form reversibly and remain stable over the course of a few minutes. This demonstrates the absence of significant photocorrosion during operation of the devices in air.

Conclusion

Overall, we demonstrate the first FTO(AZO)/ZnO/Cu_2O/PEDOT:PSS/Ni heterojunction solar cells with a device area of 1.0 cm^2. Devices are fabricated in superstrate configuration by sequential electrodeposition of ZnO and Cu_2O films from aqueous electrolytes, followed by spin-coating of PEDOT:PSS and application of nickel ink. Under AM 1.5 illumination, devices achieve up to 0.07% power conversion efficiency, 195 mV V_{OC}, and 1.28 mA/cm^2 J_{SC}. The low performance can be attributed to pinholes in the Cu_2O layers, high series resistance, and non-optimal band offsets at the ZnO/Cu_2O and Cu_2O/PEDOT:PSS interfaces. For the first time, Vibrating Kelvin Probe-SPV is used to probe the effect of the charge-selective layers on charge separation. This reveals that selective electron extraction by the ZnO ETL is not just a result of the deep ZnO valence band, which rejects Cu_2O photoholes, but also caused by a n-/p-junction which adds an electrostatic barrier for hole transfer. This barrier is observed as an inverted SPV signal under Cu_2O sub-band gap illumination. The barrier is only present in the AZO deposited films, due to the more reducing workfunction of this material compared to FTO. It explains the better performance of the AZO over the FTO devices. While the bare Cu_2O surface is electron-selective due to the presence of a hole depletion layer, the addition of PEDOT:PSS creates a hole-selective contact with Cu_2O. However, electron trapping at the Cu_2O/PEDOT:PSS interface is still prevalent and contributes to a low open circuit potential of the completed devices. Solving this problem is a topic of ongoing studies in the lab. Overall, we have described a simple and scalable pathway to Cu_2O photovoltaic cells and diagnostic tools to observe the junctions that drive charge separation in them.

Experimental Section

Zinc nitrate hexahydrate (99% metal basis, Alfa Aesar), cupric sulfate pentahydrate (Fine crystals, EM Science), sodium phosphate dibasic heptahydrate ($Na_2HPO_4 \cdot 7H_2O$, ≥ 98.0% Sigma-Aldrich), sodium hydroxide (NaOH, ≥ 97.0% Sigma-Aldrich), ethyl alcohol (CH_3CH_2OH, PG II Koptec), acetone ((CH_3CH_3CO, ≥ 99.0% Sigma-Aldrich), lactic acid ($CH_3CHCOOH$, Sigma Life Science), poly(3,4-ethylenedioxythiophene)-poly(styrenesulfonate) (PEDOT:PSS, Aldrich), DMSO (BDH, 99.9%), zinc wire (99.95% metal basis, Alfa Aesar), aluminum-doped zinc oxide (AZO, MSE), fluorine-doped tin oxide (FTO, MSI) and Triton X-100 (USB Corporation) were purchased from the respective vendors and used without further purification. Water was purified to 18 MΩ·cm resistivity using a Nanopure system.

Growth of ZnO. Electrochemical deposition of ZnO was performed in a crystallization round dish on a hotplate, using a procedure adapted from Wei et al. [13] and Ghannam et al. [35] The bath was open to air and stirred constantly at 100 rpm and heated to 70 °C. The three-electrode configuration used either 1.0 cm^2 aluminum doped zinc oxide (AZO) or fluorine doped tin oxide (FTO) as working electrodes, a 3.5 M KCl calomel reference electrode, and a Zn rod as counter electrode. Before deposition, AZO and FTO were cleaned with soap, water, ethanol, and acetone by sonication for 15 minutes in each solvent. During deposition, AZO and FTO electrodes were contacted with a Ni/Fe alligator clip. The aqueous 5.0×10^{-3} M $Zn(NO_3)_2 \cdot 6\ H_2O$ electrolyte was prepared by dissolving 0.0372 g of $Zn(NO_3)_2 \cdot 6\ H_2O$ in 25 mL H_2O. The low concentration is essential to achieving a nanorod morphology. ZnO growth was carried out in chronoamperometry mode using

a pre-step voltage of -1.2 V vs SCE for 15 s followed by a deposition voltage of -0.90 V vs SCE for 5 mins. Under these conditions, ZnO deposits as shown in **equations 1-3**. During deposition, the current was maintained at -0.35 mA cm^{-2}. During this time, the Zn counter electrode turns grey due to oxidation. Additionally, observable bubbles emerge on the surface of the working electrode, indicative of H_2 gas generation. After deposition, the electrode was removed, rinsed with water, and dried in air. Typically, one 25 mL electrolyte bath can be used to fabricate one to three 1.0 cm^2 ZnO films.

Growth of Cu_2O film. Cu_2O was electrodeposited with the same cell as above, using the 1.0 cm^2 FTO/ZnO electrode, a Pt wire counter electrode, and a 3.5 M KCl calomel reference electrode. The procedure was adapted from Wei et al.[13] The electrolyte consisted of a lactate-stabilized copper sulfate solution, which was made by dissolving 4.99 g of $CuSO_4 \cdot 5H_2O$, 13.40 g of $Na_2HPO_4 \cdot 7H_2O$, and 26.297 mL of 3 M Lactic Acid in DI water to a final solution volume of 100 mL. The pH of the electrolyte was adjusted to pH 12 by titrating in 2.0 M NaOH. Electrodeposition was carried out using chronoamperometry at a constant voltage of -0.3 V vs SCE and constant stirring of the electrolyte at 100 rpm. The temperature was fixed at 60 °C and the deposition time was 35 minutes. The chemistry of Cu_2O electrodeposition is given in **equations 4** and **5**. During deposition, the current varied from -0.8 mA cm^{-2} to -1.6 mA cm^{-2}. After deposition, the electrode was removed and rinsed, and dried in air. Typically, one 25 mL electrolyte bath can be used to fabricate two 1.0 cm^2 Cu_2O films. Cu_2O films were stored in air in the dark until further processing.

Spin Coating of PEDOT:PSS. A PEDOT:PSS film was deposited by spin-coating using a mixture of 2.5 mL PEDOT:PSS solution (3.2% w/v in water), 0.5 mL DMSO, 0.1 mL

Triton X-100 and enough water to produce a total volume of 10 mL. The solution was stored in a refrigerator (5^{o}C) before use. Spin-coating used a rate of 700 rpm for 4 minutes. Afterwards, the film was dried at 70 °C for 35 minutes on a hot plate.

Nickel metal contacts were applied using nickel conductive paint (*MG Chemicals*, 841AR Super Shield). A fine brush was used to paint a network of metal contacts, which were then dried with a heat gun at approximately 70 °C for 5 minutes. Devices were stored in air for 24 hours before measurements.

Characterization

Scanning electron micrographs (SEM) were collected on a FEI Scios Dual Beam FIB/SEM microscope with Oxford X-Max Energy Dispersive X-ray Spectroscopy (EDX) detector and an accelerating voltage of 10-30 kV. UV-Vis diffuse reflectance spectra were recorded using a Thermo Scientific Evolution 220 Spectrophotometer. Powder X-ray diffraction data were collected using a D8 Eco Advance Powder X-ray diffractometer with Lynx-EX detector. Surface photovoltage (SPV) measurements were conducted under vacuum (≤ 1.2 x 10^{-4} mbar pressure) using a vibrating gold Kelvin probe (*Delta PHI Besocke*). Samples were illuminated using a 300 W Xe lamp filtered through an *Oriel Cornerstone* 130 monochromator. SPV signals plotted in the figures equal the change of the contact potential difference (CPD) between light and dark conditions: SPV(V) = CPD(light)- CPD(dark).

Current-voltage (I-V) measurements for solar cells were performed using a *Gamry Instruments Interface 1010E* potentiostat connected to a PC. The lead for the working electrode was attached to the Ni metal contact while the leads for the counter and

reference electrode were combined and attached to the conductive substrates. For measurements under illumination, a 300 W Xe lamp was used as the light source and the beam was focused onto the solar cell using a mirror. The light intensity was calibrated to 1 sun (AM 1.5G) illumination using the current output from a commercial silicon solar cell. I-V Scans were performed from -0.5 V to 1.0 V at a 30 mV/s scan rate.

Conflicts of interest

The authors declare that they have no competing financial interests or personal relationships that could have appeared to influence the work reported in this paper.

Acknowledgements

Surface Photovoltage Measurements were supported by the U.S. Department of Energy, Office of Science, Office of Basic Energy Sciences under Award Number DOE-SC0015329.

Supporting information

Energy dispersive X-ray and photovoltaic device data.

References

1. G. Segev, J. Kibsgaard, C. Hahn, Z. J. Xu, W.-H. Cheng, T. G. Deutsch, C. Xiang, J. Z. Zhang, L. Hammarström, D. G. Nocera, A. Z. Weber, P. Agbo, T. Hisatomi, F. E. Osterloh, K. Domen, F. F. Abdi, S. Haussener, D. J. Miller, S. Ardo, P. C. McIntyre, T. Hannappel, S. Hu, H. Atwater, J. M. Gregoire, M. Z. Ertem, I. D. Sharp, K.-S. Choi, J. S. Lee, O. Ishitani, J. W. Ager, R. R. Prabhakar, A. T. Bell, S. W. Boettcher, K. Vincent, K. Takanabe, V. Artero, R. Napier, B. R. Cuenya, M. T. M. Koper, R. Van De Krol and F. Houle, *Journal of Physics D: Applied Physics*, 2022, **55**, 323003.
2. M. A. Green, E. D. Dunlop, M. Yoshita, N. Kopidakis, K. Bothe, G. Siefer and X. Hao, *Progress in Photovoltaics: Research and Applications*, 2024, **32**, 3-13.
3. S. Hadke, M. Huang, C. Chen, Y. F. Tay, S. Chen, J. Tang and L. Wong, *Chem. Rev.*, 2022, **122**, 10170-10265.
4. W. Yang, X. Zhang and S. D. Tilley, *Chemistry of Materials*, 2021, **33**, 3467-3489.
5. D. B. Mitzi, *J. Mater. Chem.*, 2004, **14**, 2355-2365.
6. D. B. Mitzi, *Advanced Materials*, 2009, **21**, 3141-3158.
7. R. Wick and S. D. Tilley, *The Journal of Physical Chemistry C*, 2015, **119**, 26243-26257.
8. A. E. Rakhshani, *Solid-State Electronics*, 1986, **29**, 7-17.
9. C. Wadia, A. P. Alivisatos and D. M. Kammen, *Environmental Science & Technology*, 2009, **43**, 2072-2077.

10. S. E. Habas, H. A. S. Platt, M. van Hest and D. S. Ginley, *Chem. Rev.*, 2010, **110**, 6571-6594.
11. L. C. Wang and M. Tao, *Electrochemical and Solid State Letters*, 2007, **10**, H248-H250.
12. T. Minami, Y. Nishi, T. Miyata and J.-i. Nomoto, *Applied Physics Express*, 2011, **4**, 062301.
13. H. Wei, H. Gong, Y. Wang, X. Hu, L. Chen, H. Xu, P. Liu and B. Cao, *CrystEngComm*, 2011, **13**, 6065-6070.
14. I. S. Brandt, M. A. Tumelero, S. Pelegrini, G. Zangari and A. A. Pasa, *Journal of Solid State Electrochemistry*, 2017, **21**, 1999-2020.
15. D. Lincot, *Thin Solid Films*, 2005, **487**, 40-48.
16. L. M. Peter, *Electrochemistry Communications*, 2015, **50**, 88-92.
17. R. Abhijit, in *Electroplating of Nanostructures*, ed. A. Mahmood, IntechOpen, Rijeka, 2015, DOI: 10.5772/61456, p. Ch. 7.
18. R. Manivannan and S. N. Victoria, *Solar Energy*, 2018, **173**, 1144-1157.
19. J. A. Switzer and G. Hodes, *MRS Bulletin*, 2010, **35**, 743-750.
20. H. M. Wei, H. B. Gong, L. Chen, M. Zi and B. Q. Cao, *The Journal of Physical Chemistry C*, 2012, **116**, 10510-10515.
21. C. Zhu and M. J. Panzer, *ACS Appl. Mater. & Interfaces*, 2015, **7**, 5624-5628.
22. D. O. Scanlon and G. W. Watson, *The Journal of Physical Chemistry Letters*, 2010, **1**, 2582-2585.
23. D. Cunningham, M. Rubcich and D. Skinner, *Progress in Photovoltaics: Research and Applications*, 2002, **10**, 159-168.

24. B. D. Yuhas and P. D. Yang, *J. Am. Chem. Soc.*, 2009, **131**, 3756-3761.

25. T. Minami, Y. Nishi and T. Miyata, *Applied Physics Express*, 2015, **8**, 022301.

26. C. X. Xiang, G. M. Kimball, R. L. Grimm, B. S. Brunschwig, H. A. Atwater and N. S. Lewis, *Energ. & Environ. Sci.*, 2011, **4**, 1311-1318.

27. L. C. Olsen, F. W. Addis and W. Miller, *Solar Cells*, 1982, **7**, 247-279.

28. J. Ouyang, C.-W. Chu, F.-C. Chen, Q. Xu and Y. Yang, *Advanced Functional Materials*, 2005, **15**, 203-208.

29. A. Dhanabalan, J. K. J. van Duren, P. A. van Hal, J. L. J. van Dongen and R. A. J. Janssen, *Advanced Functional Materials*, 2001, **11**, 255-262.

30. Z. Wang, E. S. Brown and S. Maldonado, *Chin. Chem. Lett.*, 2015, **26**, 469-473.

31. T. Dittrich, A. Belaidi and A. Ennaoui, *Sol. Energy Mater.*, 2011, **95**, 1527-1536.

32. J. You, Z. Hong, Y. Yang, Q. Chen, M. Cai, T.-B. Song, C.-C. Chen, S. Lu, Y. Liu, H. Zhou and Y. Yang, *ACS Nano*, 2014, **8**, 1674-1680.

33. Y. H. Kim, C. Sachse, M. L. Machala, C. May, L. Müller-Meskamp and K. Leo, *Advanced Functional Materials*, 2011, **21**, 1076-1081.

34. H.-Y. Chen, K. F. LoMichael, G. Yang, H. G. Monbouquette and Y. Yang, *Nat Nano*, 2008, **3**, 543-547.

35. H. Ghannam, C. Bazin, A. Chahboun and M. Turmine, *CrystEngComm*, 2018, **20**, 6618-6628.

36. A. Paracchino, J. C. Brauer, J.-E. Moser, E. Thimsen and M. Graetzel, *J. Phys. Chem. C*, 2012, **116**, 7341-7350.

37. D. Pradhan and K. T. Leung, *Langmuir*, 2008, **24**, 9707-9716.

38. J.-Y. Ho and M. H. Huang, *J. Phys. Chem. C*, 2009, **113**, 14159-14164.

39. R. Bhujel, S. Rai, U. Deka, G. Sarkar, J. Biswas and B. P. Swain, *Bull. Mater. Sci.*, 2021, **44**, 72.

40. L. Kronik and Y. Shapira, *Surf. Sci. Rep.*, 1999, **37**, 1-206.

41. T. Dittrich and S. Fengler, *Surface Photovoltage Analysis of Photoactive Materials*, World Scientific Publishing Europe Ltd., London, 2020.

42. J. Zhao and F. E. Osterloh, *J. Phys. Chem. Lett*, 2014, **5**, 782–786.

43. Y. Cheng, C. Xiao, B. Mahmoudi, R. Scheer, A. W. Maijenburg and F. E. Osterloh, *EES Catalysis*, 2023, **1**, 74-83.

44. S. Daemi, A. Kundmann, P. Cendula, K. Becker and F. E. Osterloh, *Energy Environ. Sci.*, 2023, **16**, 4530-4538.

45. S. Daemi, S. Kaushik, S. Das, T. W. Hamann and F. E. Osterloh, *J. Am. Chem. Soc.*, 2023, **145**, 25797-25805.

46. D. Menzel, A. Al-Ashouri, A. Tejada, I. Levine, J. A. Guerra, B. Rech, S. Albrecht and L. Korte, *Advanced Energy Materials*, 2022, **12**, 2201109.

47. R. M. Doughty, B. Hodges, J. Dominguez, R. Han, Z. Zhao, S. Assavachin and F. E. Osterloh, *The Journal of Physical Chemistry C*, 2020, **124**, 18426-18435.

48. R. M. Doughty, F. A. Chowdhury, Z. Mi and F. E. Osterloh, *The Journal of Chemical Physics*, 2020, **153**, 144707.

49. X. Jiang, F. L. Wong, M. K. Fung and S. T. Lee, *Applied Physics Letters*, 2003, **83**, 1875-1877.

50. M. G. Helander, M. T. Greiner, Z. B. Wang, W. M. Tang and Z. H. Lu, *Journal of Vacuum Science & Technology A*, 2011, **29**, 011019.

51. F. E. Osterloh, in *Integrated Solar Fuel Generators*, eds. Ian D Sharp, Harry A Atwater and H.-J. Lewerenz, The Royal Society of Chemistry, 2019, DOI: http://dx.doi.org/10.1039/9781788010313-00214, pp. 214-280.

52. F. E. Osterloh, *Top. Curr. Chem.*, 2015, **371**, 105-142.

53. T. Ito, T. Kawashima, H. Yamaguchi, T. Masumi and S. Adachi, *Journal of the Physical Society of Japan*, 1998, **67**, 2125-2131.

54. Z. Zhao, E. J. Willard, J. R. Dominguez, Z. Wu and F. E. Osterloh, *Journal of Materials Chemistry A*, 2019, **7**, 18020-18029.

55. M. A. Melo, Z. Wu, B. A. Nail, A. T. De Denko, A. F. Nogueira and F. E. Osterloh, *Nano Lett.*, 2018, **18**, 805-810.

56. L. H. Wong, A. Zakutayev, J. D. Major, X. Hao, A. Walsh, T. K. Todorov and E. Saucedo, *Journal of Physics: Energy*, 2019, **1**, 032001.